Flexural behavior of steel fiber-reinforced coal gangue aggregate concrete beams

Bin Cai[1], Kaiyi Li[1] and Feng Fu[2*]

[1] School of Civil Engineering, Jilin Jianzhu University, Changchun 130118, Jilin, China.
[2] School of Mathematics, Computer Science and Engineering, City, University of London, London, UK.

*Correspondence: feng.fu.1@city.ac.uk

Abstract

The flexural behavior of steel fiber-reinforced coal gangue aggregate concrete (SFCGC) and steel fiber-reinforced ordinary concrete (SFOC) beams were investigated in this study. 11 specimens were tested using four-point bending tests to investigate the effect of coal gangue replacement rate (CGRR) (0%, 50%, 100%), steel fiber volume content (SFVC) (0%, 0.5%, 1%, 1.5%), rebar ratio (0.6%, 1.17%, 1.94%), and beam height (200mm, 300mm) on the beam flexural performance. The failure modes, flexural capacities, flexural stiffness, ductility, and energy dissipation coefficient of the specimens were analyzed. In addition, the stress-strain curve of SFCGC was obtained by axial compressive tests in this study. A equations for the stress-strain relationship of SFCGC beams were obtained by data fitting. a finite element model (FEM) of SFCGC beams was established in ABAQUS. A self-programmed Python script was used to create the steel fiber model in FEM of an SFCGC beam, in which steel fibers were distributed randomly and discretely to investigate the strengthening effect of steel fibers on SFCGC beams. Finally, a comparative analysis shows good agreement in the load-deflection curves and transverse strain obtained from simulations using the established FE model and tests.

Keywords: Coal gangue; Steel fiber; Flexural performance; Load-deflection curve; Finite element; ABAQUS

1. Introduction

Coal gangue is main solid waste from the coal industry, accounting for almost a quarter of coal by production [1]. Thus far, China has accumulated more than seven billion tons of coal gangue. Due to the high yield and low utilization of coal gangue, the accumulation of coal gangue not only occupies a large amount of land but also seriously damages the environment and ecology [2,3]. The most common use of coal gangue is as an aggregate in construction projects [4]. The use of waste coal gangue for concrete production can effectively address the problem of coal gangue accumulation over a large amount of land and improve economic benefits [5-7]. It has been reported that under the same conditions, frame structures made of coal gangue have better seismic performance than concrete frame structures built using natural crushed stone while saving 6.6% of the construction cost [8]. In recent years, the material properties of coal gangue as well as the working performance, mechanical failure mechanisms [9-11], and frost resistance of coal gangue concrete using coal gangue as an aggregate replacement have been studied. Qiu et al. [12] established a freeze-thaw damage evolution model for coal gangue. Ma et al. [13] found that coal gangue as a coarse aggregate in alkali-activated gangue-slag concrete has high compressive strength and good durability and that the coal gangue content should be in the range of 30-50% when used in a freeze-thaw environment. Incorporating steel fiber or slag powder into coal gangue can optimize its mesostructure and reduce the air voids of concrete, which is conducive to the frost resistance of concrete [14]. However, coal gangue as a lightweight aggregate is characterized by high water absorption and low strength; thus, the mechanical properties and durability of coal gangue concrete are worse than those of ordinary concrete under the same conditions [15,16]. Although the mechanical properties of coal gangue concrete are inferior to those of natural aggregate concrete [17,18], coal gangue concrete can be used in practical applications [8].

Since Mangat and Hannat [19] applied the theory of composite mechanics to steel fiber reinforced concrete in the 1970s, the theoretical research and engineering applications of steel fiber reinforced concrete have developed rapidly [20]. Fibers can significantly improve the tensile strength, deformation capacity, crack resistance, and durability of ordinary concrete [21-25]. Relevant studies have shown that the incorporation of steel fibers into coal gangue concrete can optimize its mesostructure and reduce the air voids of concrete [14].

In addition, finite element (FE) analysis is also an effective method to study the structural performance of new material beam members. Gotame et al. [26] performed a nonlinear finite element analysis to evaluate the buckling behavior of corrosion-damaged reinforced concrete beams reinforced with externally bonded fibre reinforced polymer. Aghani et al. [27] performed a nonlinear finite element analysis using ABAQUS software to estimate the long-term response of the reinforced concrete beam. Xu et al. [28] proposed the preparation of highly porous ceramics using coal gangue, coal slime, and coconut palm fibers as raw materials and built an FE model of porous ceramics using ABAQUS to simulate the stress distribution and compressive strength of porous ceramics. Zhang et al. [29] presented an FE model for circular concrete-filled steel tube (CFST) short columns prepared with coal gangue based on ABAQUS, and comparison of the numerical results with experimental data showed that the coal gangue replacement rate and the confinement effect are the main factors affecting the compressive behavior of CFSTs. Previous numerical studies also revealed that the FE software ABAQUS can simulate the mechanical behavior and ultimate loads of various members with very high accuracy. However, there are few studies on FE models of steel fiber reinforced coal gangue concrete beams. To fill the research gap, this study investigated the influence of various parameters on the flexural performance of SFCGC beams with reference to the above case studies and by means of a FEM established in ABAQUS.

The flexural properties of concrete beams prepared from coal gangue aggregate were investigated in this study. Four-point bending tests were conducted on 11 beams with different values of the coal gangue replacement rate, steel fiber volume content, rebar ratio, and beam height. The measured failure modes, load-deflection curves, flexural stiffness, ductility, and energy dissipation coefficient of the specimens were analyzed. The principal structure curves and calculation equations of the steel fiber-reinforced coal gangue coarse concrete (SFCGC) beams were obtained by fitting the measurement data, and a nonlinear elastic-plastic finite element model (FEM) of SFCGC was established and validated based on the test results. The validated FEM was used to conduct a parametric study to investigate the effects of the CGRR, SFVC, and rebar ratio on the flexural load carrying capacity of SFCGC beams.

2. Experimental Tests

2.1. Mix design and basic mechanical properties of the materials

Natural gravel and coal gangue with particle diameters of 5-12 mm were used to prepare SFOC and SFCGC beams. Table 1 shows the chemical composition of coal gangue determined by an X-ray fluorescence (XRF) test. The basic material performance indices are listed in Table 2. The properties of the fibers are shown in Table 3. Corrugated steel fibers were used in this study.

Table 4 shows the mix proportion used to fabricate the specimens following JGJ55-2011 [30] and CECS38:2004 [31]. Standard test cubes with dimensions of 150×150×150 mm^3 and 100×100×300 mm^{3}were maintained under the same conditions for 28 days, and then used to perform axial compression and splitting tensile tests according to GB/T 50081-2019 [32]. Tensile strength tests were conducted on longitudinal rebar samples. The measured mechanical properties of SFOC and SFCGC are shown in Table 5, and those of rebar are shown in Table 6. The rebar used in this study originated from the construction site. It is understood that this batch of steel bars have been cold-drawn by people on the construction site, so that their strength has been improved, resulting in higher test results than theoretical results.

Table 1

Chemical composition of coal gangue.

SiO_2	Al_2O_3	Fe_2O_3	FeO	BaO	MgO	K_2O	Na_2O	TiO_2	P_2O_5	MnO
48.14	48.14	4.59	7.03	7.40	6.53	2.16	3.70	2.31	0.51	0.2

Table 2

Performance indices of shale ceramsite.

Materials	Bulk density(kg/m^3)	Water absorption(%)	Crash index(%)
Natural stone	1500	1.57	6.5
Coal gangue	1205	5.63	10.4

Table 3

Physical properties of steel fibers.

Steel fiber	Length(mm)	Width(mm)	Thickness(mm)	Equivalent diameter(mm)	Aspect ratio	Density(g/cm^3)
CSF	38	1	0.35-0.5	0.76	50	7.8

Table 4

Mixture compositions (Unit:kg/m^3).

No.	R%	v_{sf}%	CG	gravel	cement	sand	Pl	W/C
SFOC-1	0	1	0	1155.5	503.7	622.22	5.04	0.40

HSFCGC-1	50	1	577.7	577.8	503.7	622.22	5.04	0.40
SFCGC-0	100	0	1155.5	0	503.7	622.22	5.04	0.40
SFCGC-0.5	100	0.5	1155.5	0	503.7	622.22	5.04	0.40
SFCGC-1	100	1	1155.5	0	503.7	622.22	5.04	0.40
SFCGC-1.5	100	1.5	1155.5	0	503.7	622.22	5.04	0.40

Note: In the specimen names, SFOC indicates that R is 0%, that is, ordinary concrete; HSFCGC and SFCGC indicate that R is 50% and 100% respectively; and the number indicates the v_{sf}; R = CGRR; v_{sf} = SFVC, CG = the coal gangue coarse aggregate; Pl = the plasticizer; W/C = the water-cement ratio.

Table 5

Measured mechanical properties of the concrete.

No.	Axial compressive strength (MPa)	Splitting tensile strength (MPa)	Elastic modulus (GPa)
SFOC-1	47.11	3.53	34.05
HSFCGCC-1	46.62	3.51	33.96
SFCGC-0	35.87	2.44	30.00
SFCGC-0.5	42.31	2.88	33.11
SFCGC-1	46.56	3.48	33.76
SFCGC-1.5	46.83	3.61	33.14

Table 6

Basic parameters of the rebar.

Rebar type	Diameter(mm)	Yield strength(MPa)	Ultimate strength(MPa)	Elastic modulus(GPa)
HRB400	10	513	611	205
HRB400	14	453	568	205
HRB400	18	431	543	213

2.2. Specimen parameters

The specific parameters of the test beams are shown in Table 7. 11 beams were designed, including 9 SFCGC beams and 2 SFOC beams with a 25-mm-thick protective layer, where the test beam rebar details is shown in Table 8.

Table 7

Design of test beams.

No.	R%	v_{sf}%	ρ%	b/mm	h/mm	h_0/mm	L/mm	L_0/mm
SFOC-2-1	0	1	1.17	150	200	175	2000	1800
SFCGC-1-1	100	1	0.6	150	200	175	2000	1800
SFCGC-2-1	100	1	1.17	150	200	175	2000	1800
SFCGC-3-1	100	1	1.94	150	200	175	2000	1800
HSFCGC-2-1	50	1	1.17	150	200	175	2000	1800
SFCGC-2-0	100	0	1.17	150	200	175	2000	1800
SFCGC-2-0.5	100	0.5	1.17	150	200	175	2000	1800
SFCGC-2-1.5	100	1.5	1.17	150	200	175	2000	1800

SFOC-4-1	0	1	1.12	150	300	275	2000	1800
HSFCGC-4-1	50	1	1.12	150	300	275	2000	1800
SFCGC-4-1	100	1	1.12	150	300	275	2000	1800

Note: ρ = rebar ratio; b = beam section width; h = beam section height; h_0 = the effective height; L = beam length; L_0 = beam effective length. In the specimen names, the first symbol "l, 2, 3, 4" indicates 0.6%, 1.17%, 1.94%, 1.12%, respectively; and the second symbol indicates v_{sf}.

Table 8

Rebar details for all test beams.

Specimen	Longitudinal rebar		Stirrups
	Tensil rebar	Compressed rebar	
SFOC-2-1	2H14	2H8	H8@75
SFCGC-1-1	2H10	2H8	H8@75
SFCGC-2-1	2H14	2H8	H8@75
SFCGC-3-1	2H18	2H8	H8@75
HSFCGC-2-1	2H14	2H8	H8@75
SFCGC-2-0	2H14	2H8	H8@75
SFCGC-2-0.5	2H14	2H8	H8@75
SFCGC-2-1.5	2H14	2H8	H8@75
SFOC-4-1	3H14	2H8	H8@75
HSFCGC-4-1	3H14	2H8	H8@75
SFCGC-4-1	3H14	2H8	H8@75

Note: "H8", "H10", "H14", "H18" denote ribbed rebar (the rebar type HRB400) with nominal diameters of 8, 10, 14 and 18 mm, respectively. "@75" denotes the spacing between the stirrups along the test beam is 75mm.

2.3. Loading Scheme

The specimens were loaded using a 500-kN hydraulic servo pressure testing machine (Fig. 1) in a two-point symmetric manner. A 5-kN preload was first applied to the specimens, after which the load was zeroed and a new load was applied at a speed of 2 kN per minute to obtain a cumulative load of 5 kN per stage, where each stage being has held for 5 minutes. After the rebar yielded, the loading rate was adjusted to 1 kN per minute with a load increment of 2 kN per stage. The load was continuously applied until specimen failure. The transverse strain of the concrete was measured using both conventional adhesive strain gauges, and digital image correlation (DIC), on the two sides of each beam. DIC is a precise, non-contact, and non-interferometric optical method used for measuring the displacement/deformation of a structural element/material subjected to external loading. DIC is based on the principles of continuum mechanics (rigid body mechanics) [33]. The test system is shown in Fig. 2.

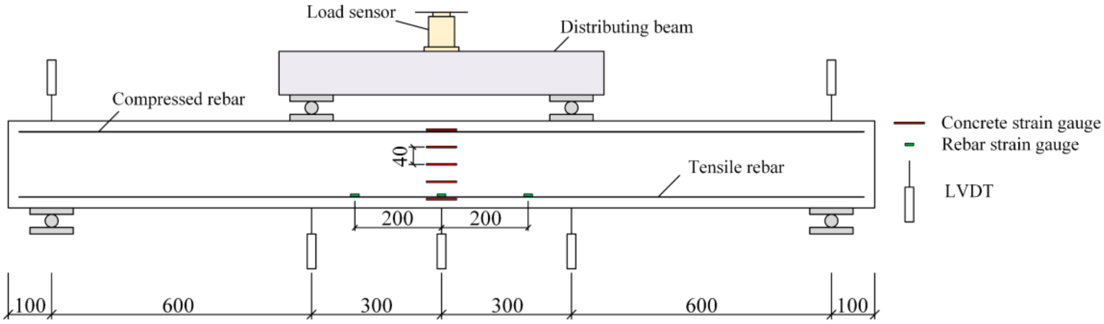

Fig. 1. Schematic diagram of loading device of the specimen.

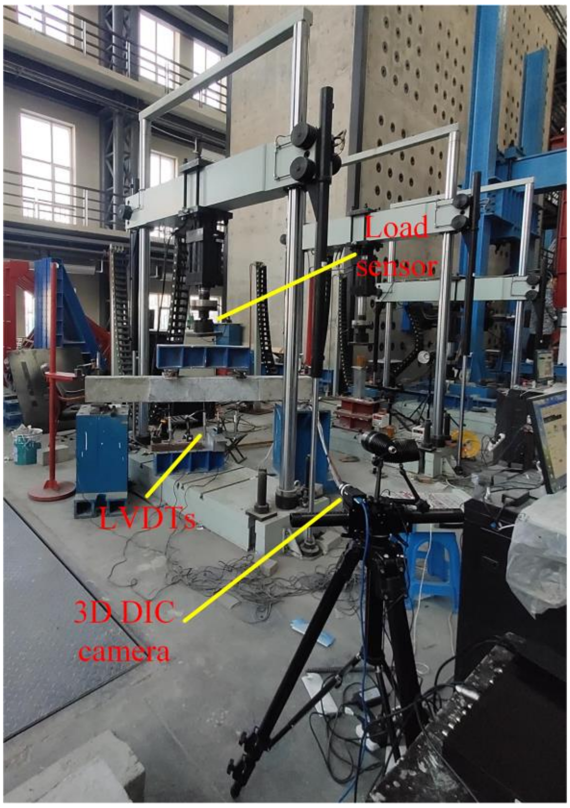

Fig. 2. DIC test preparation.

3. Test results and analysis

3.1. Experimental phenomenon

Fig. 3 shows the failure mode of SFOC-2-1 and SFCGC-2-1. The failure mode and crack pattern of the SFCGC beam were similar to those of the SFOC beam, i.e., flexural failure in both cases, as shown in Fig. 3. For the SFCGC beam, at a load of $0.3F_u$, there were clear signs of vertical cracks around the mid-span. After the formation of bending cracks around the mid-span, new vertical cracks started to propagate near the neutral layer as the load increased. During the formation of these new cracks, the cracks had already formed around the mid-span continued to propagate over the entire height of the SFCGC beam and the SFOC beam, approaching the compression zone. In addition, the already-formed cracks began to expand just below the loading point. The concrete on the top surface was damaged upon failure.

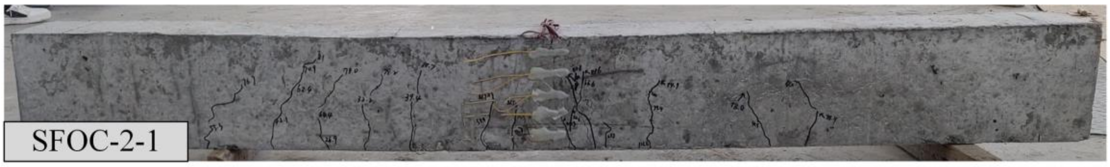

(a)

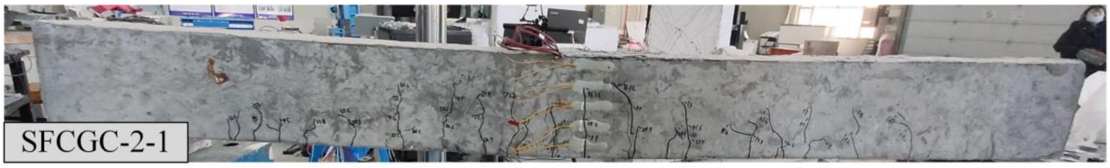

(b)

Fig. 3. Loaded state of specimens: (a) SFOC-2-1; (b) SFCGC-2-1.

3.2. Plane-section assumption

The plane-section assumption is fundamental for performing calculations based on flexural theory based on flexural theory. Fig. 4 shows the distribution of the concrete strain along the section height for different CGRRs. The concrete strain is approximately linear in the section height at all loading levels, which is consistent with the plane-section assumption. The height of the cross-sectional neutral axis is slightly lower for SFCGC beam than SFOC beam under the same loading level.

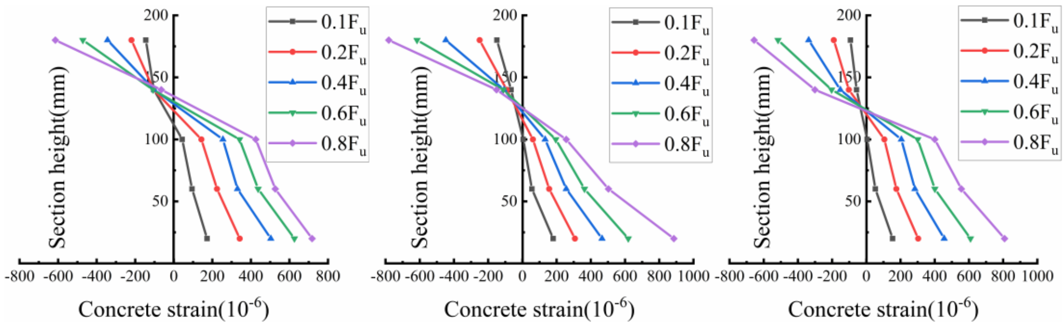

(a) (b) (c)

Fig. 4. Distribution of the concrete strain along the section height under different CGRRs: (a) SFOC-2-1; (b) HSFCGC-2-1 and (c) SFCGC-2-1.

3.3. Load-deflection curve

Fig. 5 shows the load-deflection curves of the 11 specimens. In the initial stage of loading, the specimen is in the elastic stage, and hence, the deflection basically increases linearly with the load. After concrete cracking, the first turning point appears in the load-deflection curve, leading to a decrease in the flexural stiffness and an increase in the cracks and deflection of the specimen. As the tensile rebars yielded, the second turning point appears in the load-deflection curve. Accordingly, the flexural stiffness of the specimen decreases sharply and its deflection increases rapidly. When the load reaches the peak, the concrete in the compression zone is crushed, and the specimen lost its bearing capacity.

Table 9 shows the test results of the specimens. As the beam depth increases from 200 mm to 300 mm, the bearing capacity and flexural stiffness of both SFCGC and SFOC beam increase. With increasing CGRR, there is a relatively small reduction in the cracking load of the specimens of 8.8% on average, and relatively large reductions in the yield and ultimate loads of 12.1% and 13.3% on average, respectively. With increasing SFVC, the development of cracks in the SFCGC beam is suppressed, thus substantially increasing the cracking load of the SFCGC beam. The increase in the cracking load of the specimen reaches 58.6% at 1% SFVC, and then slows beyond 1% SFVC.

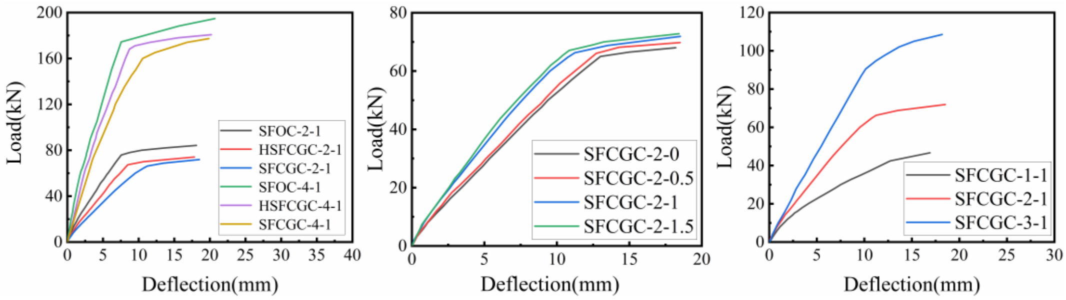

(a) (b) (c)

Fig. 5. Load-deflection curve of specimens under different effects: (a) CGRR; (b) SFVC and (c) Rebar ratio.

Table 9

Test result of specimens.

Beam specimens	F_{cr}/kN	ω_{cr}/mm	F_y/kN	ω_y/mm	F_u/kN	ω_u/mm	F_{cr}/F_u	K_0(kN/mm)	μ_ω	β
SFOC-2-1	25.50	1.97	76.00	7.65	84.23	18.11	0.30	11.30	2.37	1.53
SFCGC-1-1	15.20	2.67	42.47	12.47	46.67	16.91	0.32	5.19	1.35	1.29
SFCGC-2-1	21.57	2.87	66.27	11.24	71.90	18.52	0.30	7.14	1.65	1.39
SFCGC-3-1	27.80	2.82	90.47	10.14	108.53	18.18	0.27	9.34	1.79	1.31
HSFCGC-2-1	24.93	2.71	67.33	8.48	74.07	17.82	0.33	8.86	2.10	1.47
SFCGC-2-0	13.60	2.17	65.00	13.01	68.00	18.20	0.20	5.60	1.40	1.30
SFCGC-2-0.5	18.34	2.76	66.07	12.72	69.77	18.50	0.26	5.87	1.45	1.32
SFCGC-2-1.5	23.17	2.96	67.07	10.85	72.81	18.42	0.32	7.43	1.70	1.40
SFOC-4-1	64.50	2.10	174.43	7.55	194.75	20.70	0.33	28.63	2.74	1.57
HSFCGC-4-1	64.10	2.56	168.13	8.71	180.70	20.20	0.35	23.54	2.32	1.55
SFCGC-4-1	63.20	3.12	160.04	10.56	177.33	19.85	0.35	20.44	1.88	1.45

Note: F_{cr} = the cracking load; ω_{cr} = the cracking deflection; F_y = the yield load; ω_y = the yield deflection; F_u = the ultimate load; ω_u = the ultimate deflection; K_0 = the initial stiffness; μ_ω = the ductility; and β = the energy dissipation coefficient.

3.4. Load-rebar strain curve

The load-rebar strain curves of the specimens are shown in Fig. 6. The load-rebar strain curve of each beam specimen is similar to its load-deflection curve. The rapid increase in the average postcracking rebar strain is found to depend on tensile rebar ratio. The average rebar strain increases rapidly with the increase in rebar ratio. In addition, the rebar strain decreases as the SFVC increases, because the steel fibers bore a portion of the tension after the beam cracked, thereby reducing the rebar stress at the same load level, and decreasing the rebar strain. With the increase in CGRR, the rebar strain increases slightly under the same load level.

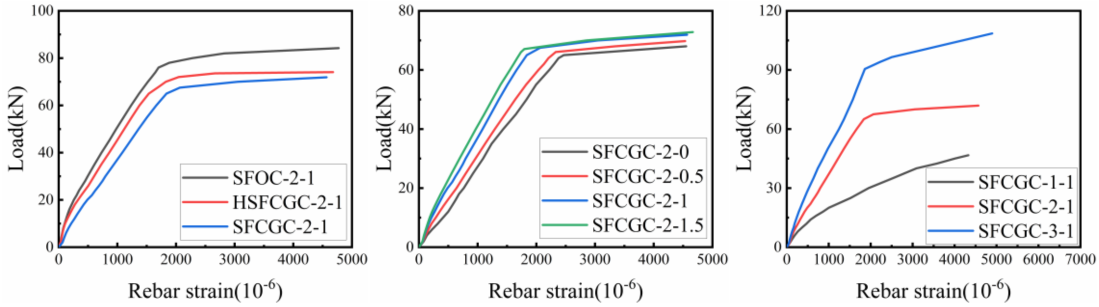

(a) (b) (c)

Fig. 6. Load-rebar strain curve under different effects: (a) CGRR; (b) SFVC and (c) Rebar ratio.

4. Analysis of influencing factors

4.1. Flexural capacity

The specimen bearing capacity decreases considerably with increasing CGRR (Fig. 7(a)), This is due to the fact that the elastic modulus of SFOC is greater than SFCGC (Table 5). With increasing SFVC, the specimen bearing capacity increases but is not much (Fig. 7(b)), which is due to the slightly increase compressive strength of the specimen by mixing steel fiber (Table 5). And the specimen bearing capacity rise dramatically with increasing rebar ratio (Fig. 7(c)).

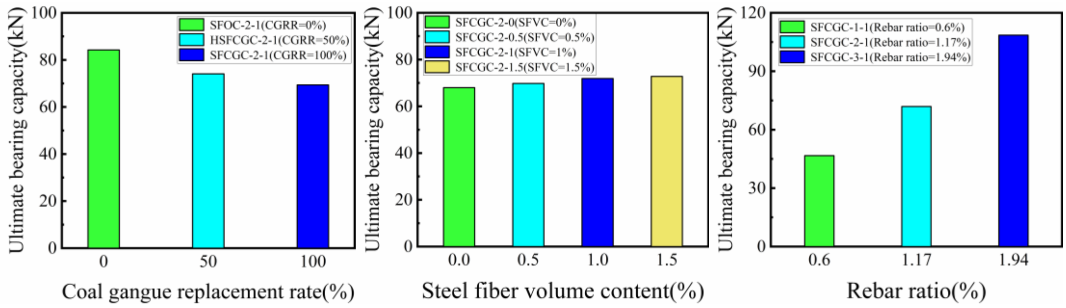

(a) (b) (c)

Fig. 7. Effects of the investigated variables on bearing capacity: (a) CGRR; (b) SFVC and (c) Rebar ratio.

4.2. Stiffness degradation

The secant stiffness at the point corresponding to $0.4F_u$ in the ascending section of the load-deflection curve is consistently taken as the initial stiffness in this study, and the results are shown in Table 9. Fig. 8 shows how the CGRR, SFVC, and rebar ratio affect the initial stiffness (denoted by K_0) of the specimen for SFOC-2-1, SFCGC-2-0, and SFCGC-1-1. The initial stiffness of the specimen gradually decreases with increasing CGRR and gradually increases with the SFVC and rebar ratio.

Fig. 9 shows how the CGRR, SFVC, and rebar ratio affect the degradation of the specimen stiffness, where K_0 represents the flexural stiffness at a specimen loading of 0.05 F_u. Fig. 9(a) and Table 8 indicate that the stiffness begins to degrade when the load reached approximately 10 kN. As the load increases from $0.05F_u$ to $0.67F_u$, the instantaneous stiffness K of SFOC-2-1, HSFCGC-2-1, and SFCGC-2-1 degrade by 35.5%, 36.3%, and 38%, respectively. These results show that the higher the CGRR is, the faster the stiffness degradation and crack development of the SFCGC beam are, because the lower elastic modulus of the coal gangue aggregate compared to that of natural crushed stone, rapidly reduces the cross-sectional stiffness of the member. Fig. 9(b) shows that the incorporated steel fibers delays the stiffness degradation of the member to a certain extent, and when the load increases to approximately 23 kN (0.3 F_u), the steel fibers no longer play a pronounced role in delaying the stiffness degradation of the member, which is because the member at this moment had entered a crack development stage and the role of steel fibers in limiting the cracking of the member is weakened. Fig. 9(c) shows that increasing the rebar ratio slows down the rate of stiffness degradation of the SFCGC beams given the same cross-section.

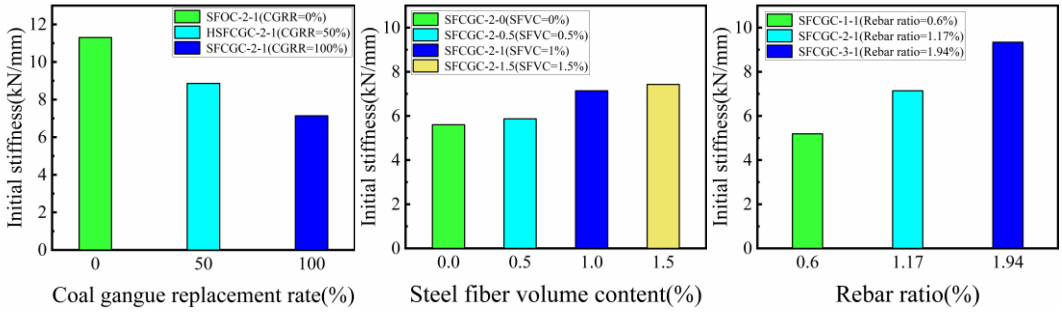

(a) (b) (c)

Fig. 8. Effects of the investigated variables on the initial stiffness: (a) CGRR; (b) SFVC and (c) Rebar ratio.

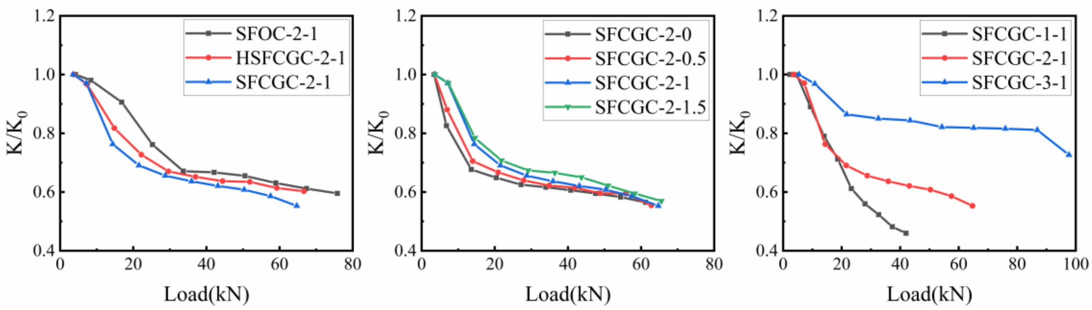

(a) (b) (c)

Fig. 9. Rigidity degenerations of specimens under different effects: (a) CGRR; (b) SFVC and (c) Rebar ratio.

4.3. Ductility analysis

The deflection ductility coefficient was used as a measure of the ductility of the specimen in this study and was calculated as follows:

$$\mu_{\omega} = \frac{\omega_{u}}{\omega_{y}} \tag{1}$$

where ω_u is the peak mid-span deflection, ω_y is the mid-span deflection corresponding to yield point, and the value is determined by the energy equivalence method (Fig. 10).

The ductility of each specimen was calculated with Equation (1), and the results are outlined in Table 9. Fig. 11 shows the effects of the CGRR, SFVC, and rebar ratio on the specimen ductility. The specimen ductility decreases by 11.4% and 30.4% at CGRRs of 50% and 100%, respectively. This result implies that the specimen ductility decreased increasingly rapidly with increasing CGRR. The specimen ductility trends upward with the SFVC, with an average increase of 13.2%. The specimen ductility increases significantly with the rebar ratio.

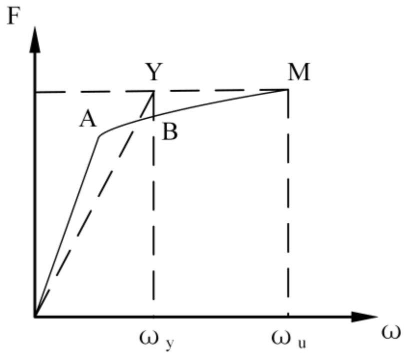

Fig. 10. Schematic diagram for calculating ductility coefficient.

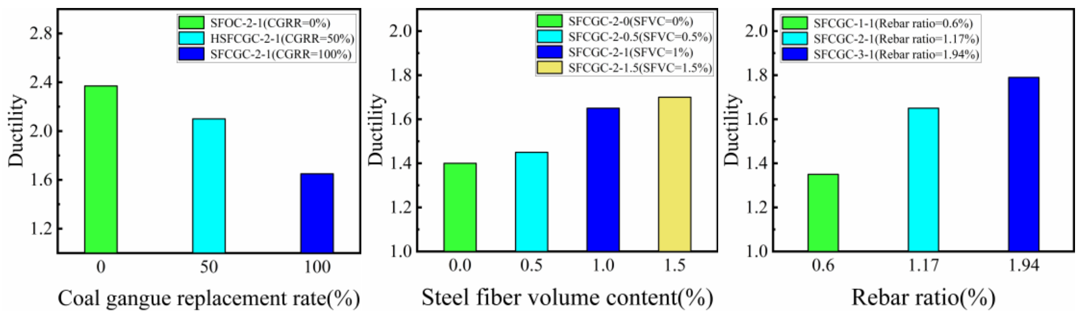

(a) (b) (c)

Fig. 11. Effects of the investigated variables on the specimen ductility: (a) CGRR; (b) SFVC and (c) Rebar ratio.

4.4. Energy dissipation coefficient analysis

The capacity of a member to dissipate energy determines the level of protection provided to a building in an earthquake. In this study, the magnitude of the energy dissipation of the specimen was denoted by β:

$$\beta = \frac{S_{OCAB}}{S_{\mathrm{OAB}}} \tag{2}$$

where S_{OCAB} is the area enclosed by the load-deflection curve and the coordinate axis at the peak load, which is the actual energy dissipation, S_{OAB} is the area of the triangle enclosed by the origin, the ultimate load point and the coordinate axis (Fig. 12).

The energy dissipation coefficient of each specimen was calculated according to Equation (2), and the results are given in Table 9. Fig. 13(a) shows that the energy dissipation of the specimens decreases slightly (by 10%) with increasing CGRR. As the coal gangue aggregate contained more cracks and pores than natural gravel, compression, and closure of cracks during loading, increase the energy absorption of the specimen and lower the energy dissipation. Fig. 13(b) shows that the energy dissipation coefficient of SFCGC beams increases slightly with increasing SFVC. As shown in Fig. 13(c), as the rebar ratio increases, the energy dissipation coefficient does not change appreciably and first increased and then decreased overall. Therefore, the use of a high rebar ratio both improves the bearing capacity and reduces the energy dissipation of SFCGC beams.

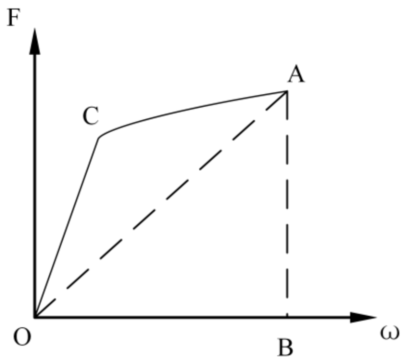

Fig. 12. Calculation of the energy dissipation coefficient.

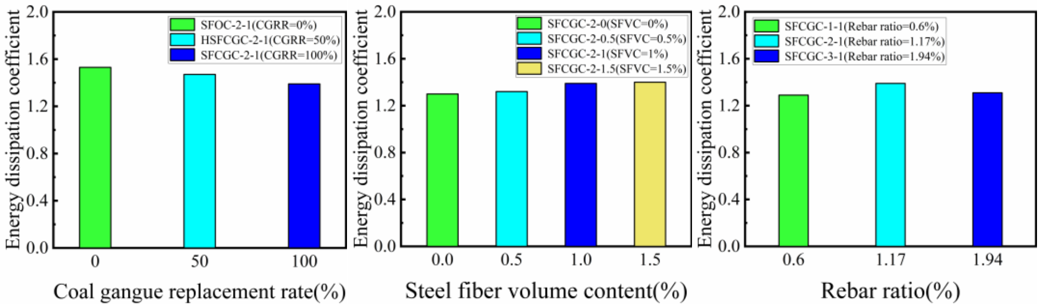

(a) (b) (c)

Fig. 13. Effects on the investigated variables on the energy dissipation coefficient of the specimens: (a) CGRR; (b) SFVC and (c) Rebar ratio.

4.5. Calculation of the cracking load

The cracking load (F_{cr}) can be calculated is as follows [37]:

$$F_{cr} = \frac{2M_{cr}}{L} \tag{3}$$

$$M_{cr} = f_t b(h - x_{cr})\left(\frac{h - x_{cr}}{2} + \frac{2x_{cr}}{3}\right) + 2\alpha_E f_t A_s\left(h - \frac{x_{cr}}{3}\right) \tag{4}$$

$$x_{cr} = \frac{1 + \frac{2\alpha_E A_s}{bh}}{1 + \frac{\alpha_E A_s}{bh}} \cdot \frac{h}{2} \tag{5}$$

where M_{cr} is the cracking moment of the specimen; L is the pure bending region of the beam (=600mm in this study); f_t is the tensile strength of concrete; h is the beam height; and x_{cr} is the effective depth of the concrete compression zone when concrete cracks occur; and α_E is the ratio of elastic modulus of rebar to that of concrete.

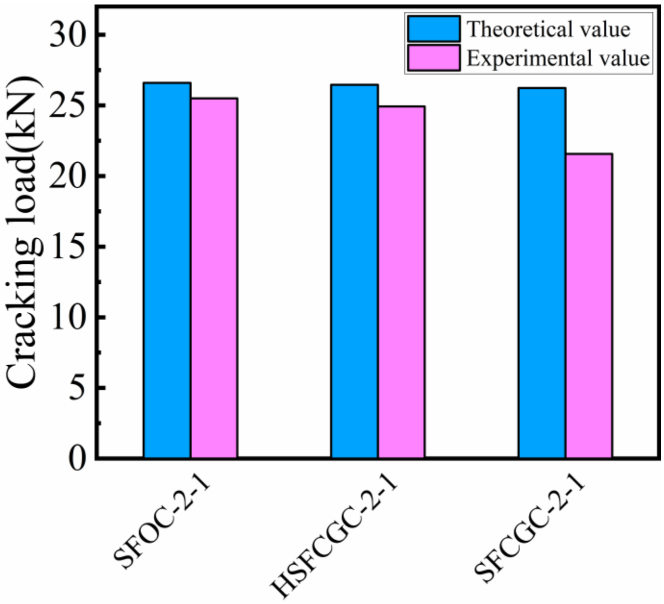

Fig. 14. Comparison between theoretical value and experimental value on the cracking load of the specimens on different CGRR

Fig. 14 exhibits the comparision between the theoretical value and experimental value on the cracking load of the beam specimens with an SFVC of 1% and a rebar ratio of 1.17% and different CGRR. It can be seen that the error between the two is small, and the calculation accuracy of the formula is good. It is proved that Equation (3) and Equation (4) can well predict the cracking load and moment of SFCGC beam.

4.6. Calculation of the ultimate load

The ultimate load (F_u) can be calculated is as follows [37]:

$$F_u = \frac{2M_u}{L} \tag{6}$$

$$M_u = f_y A_s \left(h_0 - \frac{x}{2} \right) \tag{7}$$

$$x = \frac{f_y A_s}{\alpha_1 f_c b} \tag{8}$$

where M_u is the ultimate moment of the specimen; α_1 is a coefficient related to concrete strength (i.e. 1.0 for concrete grades ≤ C50, and 0.94 for concrete grades ≥ C80); f_c is the axial compressive strength of concrete cube; and x is the concrete compression zone depth, assuming the equivalent rectangular block.

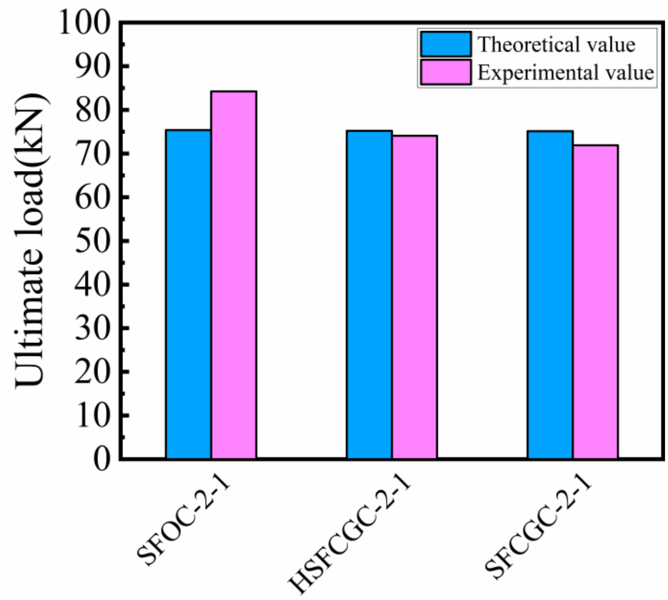

Fig. 15. Comparison between theoretical value and experimental value on the cracking load of the specimens on different CGRR

Fig. 15 exhibits the comparision between the theoretical value and experimental value on the ultimate load of the beam specimens with an SFVC of 1% and a rebar ratio of 1.17% and different CGRR. It can be seen that the error between the two is small, and the calculation accuracy of the formula is good. It is proved that Equation (6) and Equation (7) can well predict the ultimate load and moment of SFCGC beam.

6. Finite element simulation

6.1. FEM model and meshing

The core SFCGC was modeled using eight-node 3D solid elements with reduced integration (C3D8R) [34]. The rebar and steel fiber were constructed using T3D2 elements. T3D2 is a 2-node linear displacement element, where each node has three translational degrees of freedom. The specifications of the overall model are shown in Fig. 16. Based on a convergence analysis, the mesh size of all beams was chosen as 20mm, where the mesh distribution of the model is shown in Fig. 17.

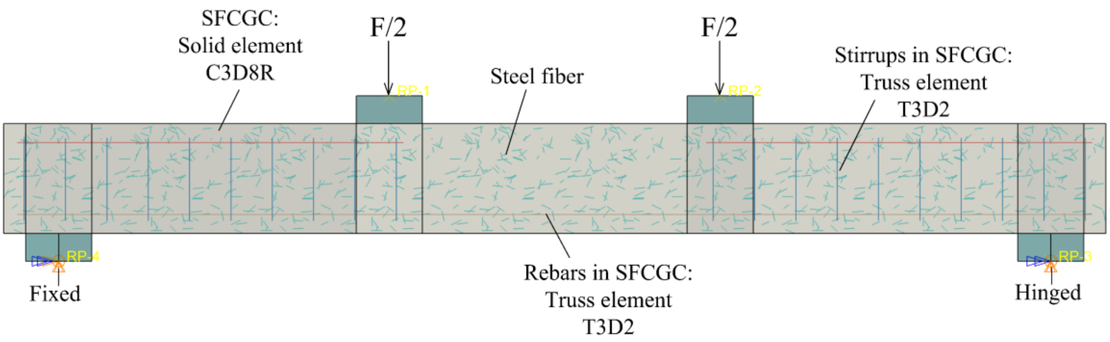

Fig. 16. FEM.

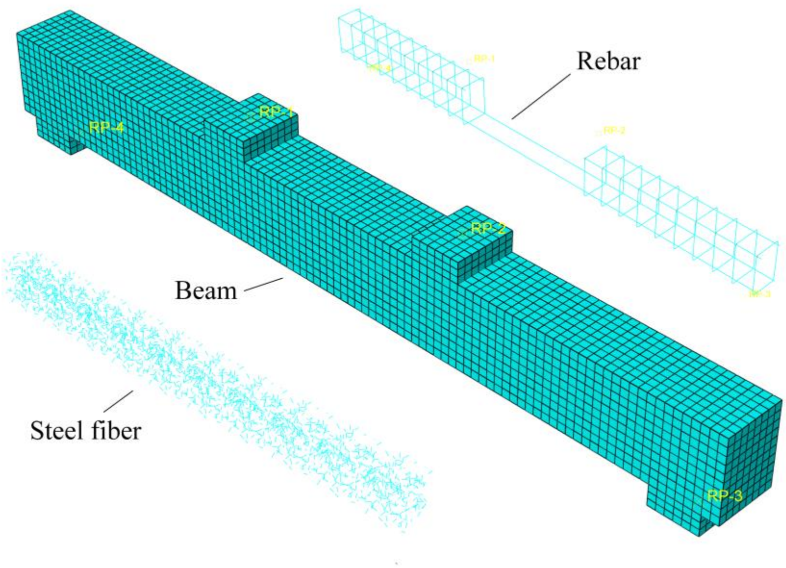

Fig. 17. FEM meshing.

6.2. Model parameters

6.2.1. Constitutive model of concrete

The stress-strain curves under tension and compression are defined differently within the concrete damaged plasticity (CDP) model. The stress-strain curve of concrete under uniaxial compression obtained by uniaxial compression tests on prisms is shown in Fig. 18, and its overall shape is found similar to that of ordinary concrete. Therefore, the full stress-strain curve of ordinary concrete described by Equation (9) [35] was used to fit the constitutive equation of SFCGC.

$$y=\begin{cases} ax+(3-2a)x^2+(a-2)x^3, 0\le x\le 1 \\ \dfrac{x}{b(x-1)^2+x}, x>1 \end{cases} \tag{9}$$

where a is the parameter for fitting the rising section of the stress-strain curve, reflecting the change of concrete deformation modulus; b is the parameter for fitting the declining section of the stress-strain curve, reflecting the size of the area of the declining section curve; x is the ratio of strain to peak strain (i.e. $x=\varepsilon/\varepsilon_p$); and y is the ratio of stress to peak stress (i.e. $y=\sigma/\sigma_p$).

The parameters a and b were obtained by curve fitting, as shown in Table 10. Both a and b decrease as CGRR increases, indicating that the higher the CGRR is, the lower the elastic modulus and plastic deformation capacity are, which is consistent with the data presented in Table 5. As the SFVC increases, a increases and b decreases because in the ascending section of the curve, the cracks are in the stable development stage, and the steel fibers across the cracks play a role in blocking cracks and slowing crack propagation. Thus, a higher SFVC results in a stronger crack-blocking effect, a fuller curve, and a larger a. In the descending section of the curve, the cracks are in the instability and propagation stage. The pull-out force on the steel fibers between the cracks slows the disintegration of the cement paste, flattening the descending section of the curve. Thus, increasing the SFVC increases the number of fibers between cracks, resulting in a flatter curve and a smaller b. Based on the trend of parameters a and b, a fitted regression analysis of a and b was performed using a linear equation to obtain the fitting curve shown in Fig. 19, and Equations (10)-(13) show the fitting parameters a and b for the obtained constitutive equation of the SFCGC under uniaxial compression as a function of the CGRR and SFVC.

Since it is necessary to investigate the concrete cracking and characterize the crack development after concrete cracking, the constitutive equation of SFCGC under tension is determined using the energy criterion (i.e., stress-fracture energy) for concrete failure [36].

The CDP model requires five additional parameters: the flow potential eccentricity; a viscosity parameter that is a measure of the viscoplastic regularization (μ); the ratio of the second stress invariant for the tensile meridian to that for the compressive meridian, such that the maximum principal stress is negative (K_c); the ratio of the initial equibiaxial compressive yield stress to the initial uniaxial compressive yield stress (σ_{b0}/σ_{c0}) and the dilation angle in degrees (ψ). The corresponding parameter values were set as 0.1, 0.0005, 0.6667, 1.16, and 30˚ for SFCGC material [29].

$$a=-0.001371R+0.6373 \tag{10}$$

$$b=-0.05212R+11.82 \tag{11}$$

$$a=0.08912v_{sf}+0.4051 \tag{12}$$

$$b=-5.825v_{sf}+12.72 \tag{13}$$

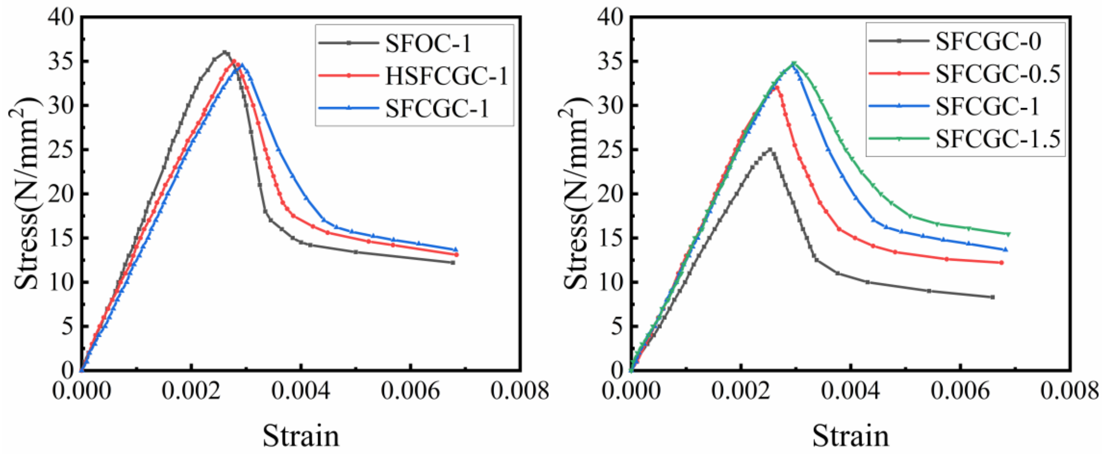

(a) (b)

Fig. 18. Effect of compressive stress-strain curves of the SFCGC: (a) CGRR and (b) SFVC.

Table 10

Fitting parameters of the uniaxial compressive constitutive equation of concrete.

parameters	SFOC-1	HSFCGC-1	SFCGC-1	SFCGC-0	SFCGC-0.5	SFCGC-1.5
a	0.63	0.59	0.49	0.39	0.46	0.54
b	11.36	10.14	6.481	12.6	10.37	4.30

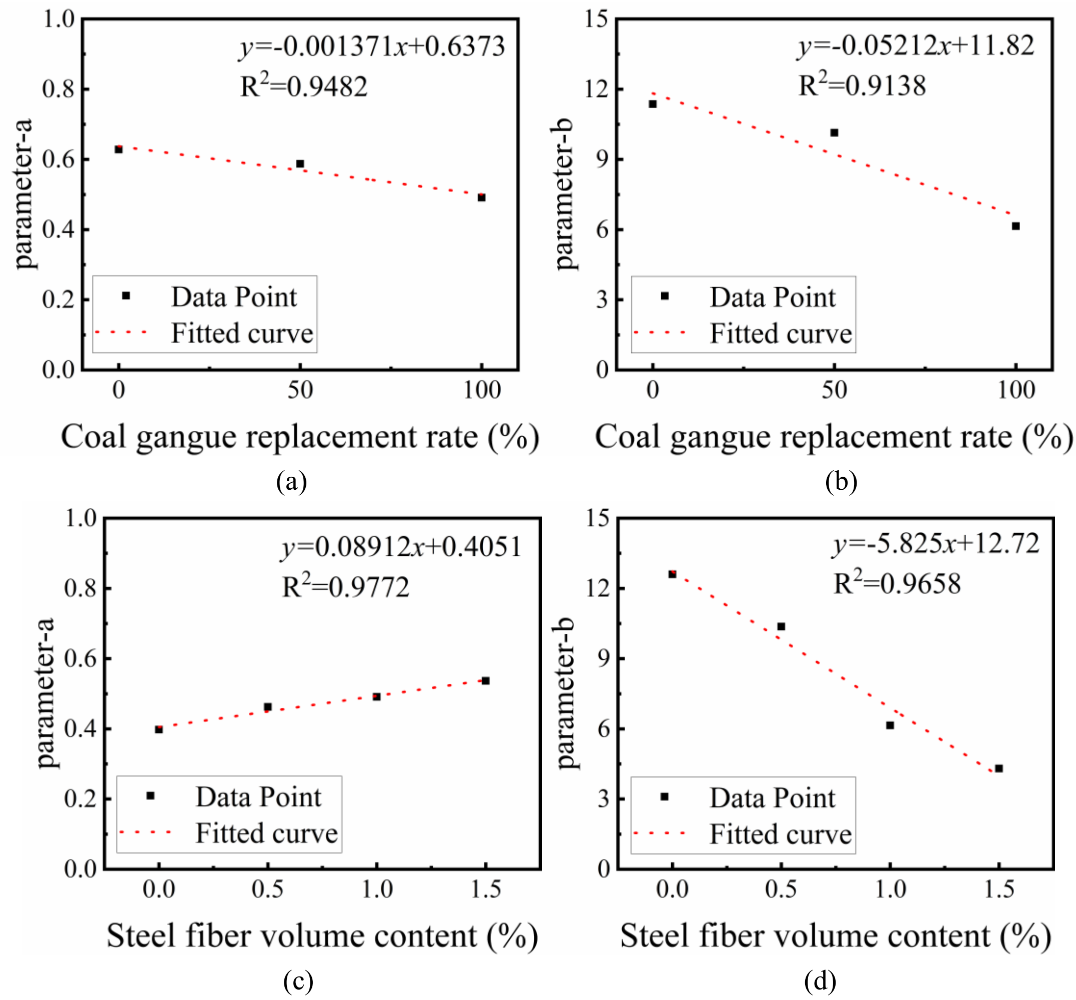

Fig. 19. Fitted curves to relate the parameters *a* and *b* with the CGRR and SFVC: (a) Fitted curve of the relationship between the parameter a and the CGRR; (b) Fitted curve of the relationship between the parameter b and the CGRR; (c) Fitted curve of the relationship between the parameter a and the SFVC and (d) Fitted curve of the relationship between the parameter b and the SFVC.

6.2.2. Constitutive model of rebar

The damage inflicted on the reinforced concrete elements results in the deformation of the rebar and steel fiber mainly remaining in the yield plateau range. Neglecting yield hardening, two fold ideal elastic-plastic model (Fig. 20) according to GB 50010-2010 [37] was used to describe the steel fibers and rebar, where the stress-strain relationship is shown in Equation (14):

$$\sigma_\mathrm{p} = \begin{cases} E_\mathrm{s}\varepsilon_\mathrm{s}, \varepsilon \le \varepsilon_\mathrm{y} \\ f_y, \varepsilon > \varepsilon_\mathrm{y} \end{cases} \tag{14}$$

where σ_p = rebar stress, ε_s = rebar strain, ε_y = the yield strain of rebar, f_y = the yield strength of the rebar, and E_s = the elastic modulus of rebar.

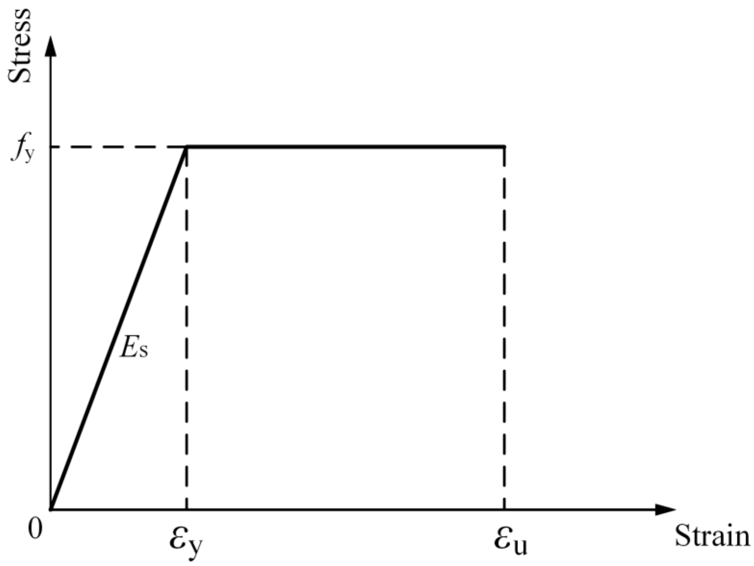

Fig. 20. Stress-strain relationship for rebars.

6.2.3. Steel fiber model

The computer code for the randomly distributed steel fiber model was written in Python and imported into ABAQUS. An independent steel fiber model was formed by setting the length of steel fibers, the size of a specific region, and the number of steel fibers in that region. According to the dimensions of the specimen in this study, a beam was divided into 10 equal parts, with the length, width, and height of each region being 200 mm, 150 mm, and 200 mm, respectively. Fig. 21 is a flow chart showing the modeling procedure for the steel fiber, which was finally embedded in the FEM of the SFCGC beam, as shown in Fig. 16. After the modeling was completed, the corresponding material properties were assigned to the steel fibers.

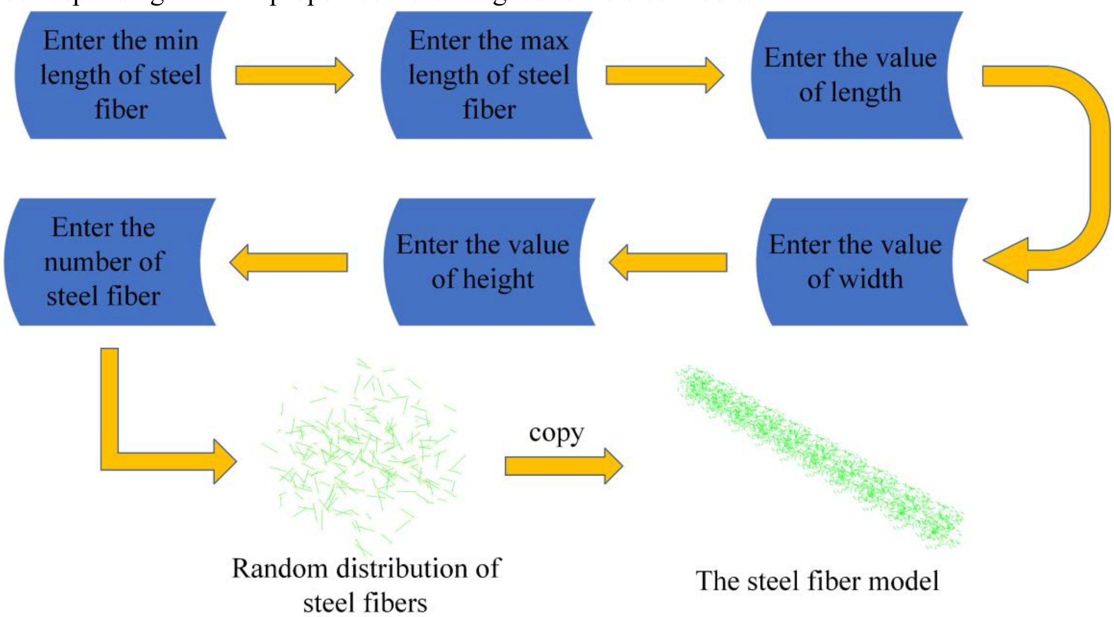

Fig. 21. Flow chart for the modeling procedure for the steel fibers.

6.3. Interaction

Embedded constraints were applied between the rebar cage and the SFCGC beam as well as between the steel fibers and the SFCGC beam. The SFCGC beam was the main region, and the rebar cage and steel fibers were separate built-in regions. Binding constraints were set between the supports and the beam. The four steel block supports were coupled to RP1, RP2, RP3, and RP4, respectively, so that the degrees of freedom (DOFs) of the supports were controlled by these four constraint points.

6.4. Boundary conditions and load application

The boundary conditions of the FEM of the SFCGC beam prepared with coal gangue aggregate were chosen to be consistent with the test conditions. Simply supported boundary conditions were applied to the supports. The centers of the two beam supports were set as RP3 and RP4, respectively (Fig. 16), and the two supports were set as rigid bodies. The DOFs of RP3 were U1=U2=0, and the DOFs of RP4 were U1=U2=U3=0. External loads were applied to the two steel blocks at the top of the beam by displacement.

6.5. Model validation

6.5.1. The validation of the load-deflection curves

To ensure the reliability of the developed numerical model, the simulation results obtained using the FEM were compared with the experimentally obtained values in Fig. 22 and Table 11. The difference between the simulated and experimental load-deflection curves over the entire loading process is approximately 10%: this good agreement shows that the flexural performance of SFCGC beams can be effectively simulated using the developed modeling method.

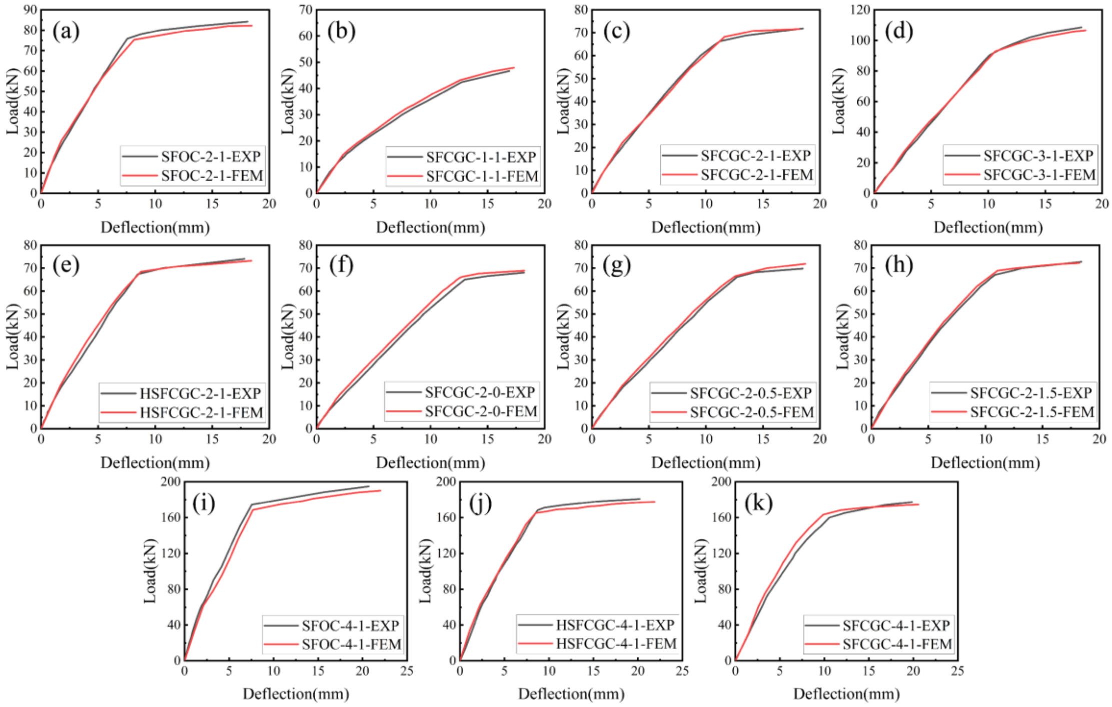

Fig. 22. The comparison of the load-deflection curves calculated by the FEM with the experimental results.

Table 11

Simulated and tested results of load and deflection.

Specimens	F_{cr}(kN)			ω_{cr}(mm)			F_y(kN)			ω_y(mm)			F_u(kN)			ω_y(mm)		
	F_{exp}	F_{simu}	F_{exp}/ F_{simu}	ω_{exp}	ω_{simu}	ω_{exp}/ ω_{simu}	F_{exp}	F_{simu}	F_{exp}/ F_{simu}	ω_{exp}	ω_{simu}	ω_{exp}/ ω_{simu}	F_{exp}	F_{simu}	F_{exp}/ F_{simu}	ω_{exp}	ω_{simu}	ω_{exp}/ ω_{simu}
SFOC-2-1	25.50	26.00	0.98	1.97	1.79	1.10	75.81	75.27	1.01	7.65	8.15	0.94	84.23	82.21	1.02	18.11	18.47	0.98
SFCGC-1-1	15.20	14.71	1.03	2.67	2.32	1.15	42.47	43.17	0.98	12.75	12.59	1.01	46.67	47.89	0.97	16.91	17.32	0.98
SFCGC-2-1	21.57	22.12	0.98	2.87	2.68	1.07	66.27	68.21	0.97	11.24	11.63	0.97	71.90	71.63	1.00	18.52	18.21	1.02
SFCGC-3-1	27.80	26.83	1.04	2.82	2.57	1.10	90.47	92.84	0.97	10.14	10.61	0.96	108.53	106.49	1.02	18.19	18.54	0.98
HSFCGC-2-1	24.93	24.64	1.01	2.71	2.36	1.15	67.33	68.43	0.98	8.48	8.75	0.97	74.07	73.24	1.01	17.82	18.43	0.97
SFCGC-2-0	13.60	12.95	1.05	2.17	1.72	1.26	65.00	66.18	0.98	13.01	12.77	1.02	68.00	68.87	0.99	18.20	18.22	1.00
SFCGC-2-0.5	18.34	18.63	0.98	2.76	2.64	1.05	66.07	66.52	0.99	12.72	12.59	1.01	69.77	71.88	0.97	18.50	18.71	0.99
SFCGC-2-1.5	23.17	22.24	1.04	2.96	2.67	1.11	67.07	68.88	0.97	10.85	11.06	0.98	72.81	72.26	1.01	18.42	18.22	1.01
SFOC-4-1	64.50	61.63	1.05	2.10	2.09	1.00	174.43	168.46	1.04	7.55	7.66	0.99	194.75	190.03	1.02	22.70	22.00	1.03
HSFCGC-4-1	64.10	62.89	1.02	2.56	2.28	1.12	168.13	165.06	1.02	8.71	8.50	1.02	180.70	177.42	1.02	20.20	21.86	0.92
SFCGC-4-1	63.20	60.49	1.04	3.12	2.59	1.20	160.04	163.28	0.98	10.56	9.87	1.07	173.30	174.44	1.02	19.85	20.57	0.96

Note: F_{exp} = the test result of the load; F_{simu} = the simulated result of the load; ω_{exp} = the test result of the deflection; ω_{simu} = the simulated result of the deflection.

6.5.2. The validation of the transverse strain

The FEM developed in this study can also be used to take into account differences between the tensile and compressive properties of materials and simulate irreversible degradation of the stiffness due to damage. Two damage coefficients, DAMAGEC and DAMAGET, were defined according to GB 50010-2010 [37] to reflect the development of cracks. Fig. 23(a) presents a contour plot of the transverse strain of SFCGC beam processed by DIC software, and Fig. 23(b) shows the development of cracks in the SFCGC beam (CGC-2) and the corresponding FEM. The crack development is effectively simulated using the FEM. The crack strain development locations of the two are similar, with the maximum crack strain occurring near the loading point.

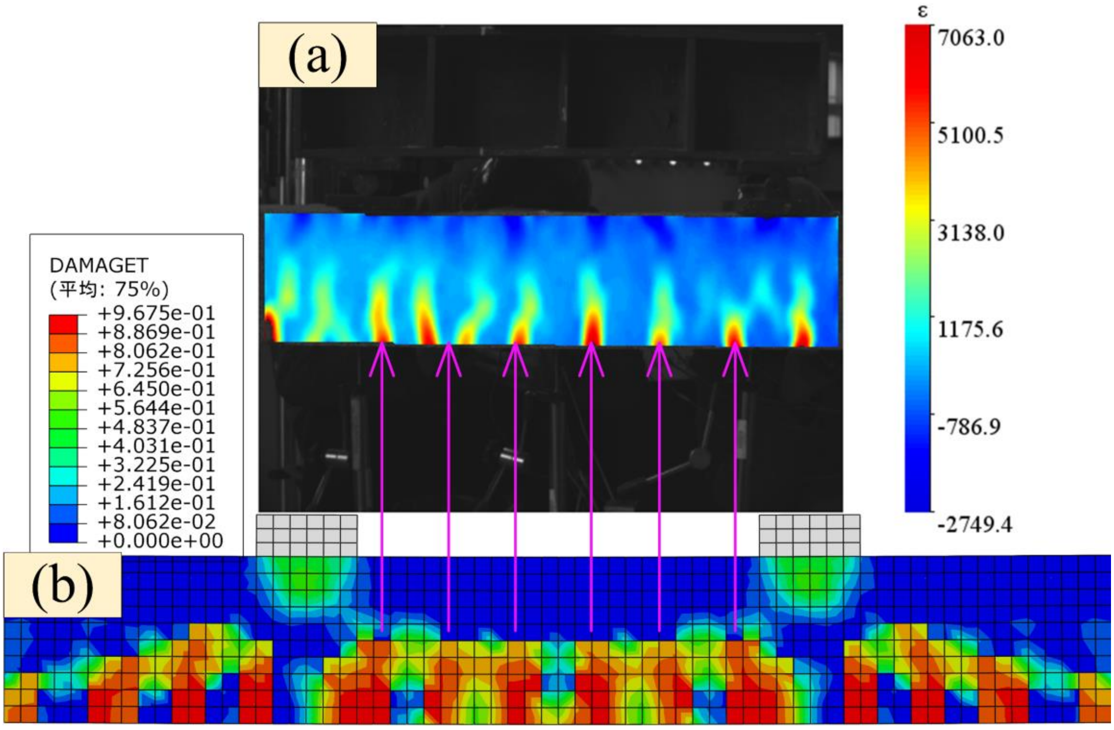

Fig. 23. Comparison between experimental and simulated results.

6.6. Parametric study

The validated FEM was used to carry out a parametric study to quantify the effect of different parameters on the flexural performance of SFCGC beams.

6.6.1. Coal gangue replacement rate

The simulation load-deflection curve of elements with different CGRRs is shown in Fig. 24. The results present in Fig. 22 and Table 11 shows that compared with the results for SFOC beams, the cracking load, yield load, and ultimate load of SFCGC beams decrease by 14.9%, 9.4%, and 12.9%, respectively, for 100% CGRR and by 5.2%, 9.1%, and 11%, respectively, for 50% CGRR;

however, the CGRR does not have a significant effect on the ultimate displacement.

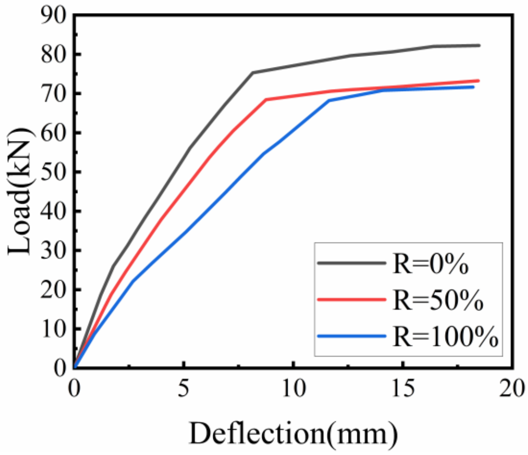

Fig. 24. Simulation results obtained for different CGRRs.

6.6.2. Steel fiber volume content

The flexural performances of SFCGC beams with different SFVCs (0, 0.5%, 1%, 1.5%, and 2%) were compared. The load-deflection curves are shown in Fig. 25. Compared with the results obtained for beams without steel fibers, increasing the SFVC has a significant influence on the cracking load but a minimal impact on the yield load, ultimate load, and ultimate displacement of the member. In particular, the ultimate displacement and ultimate load do not change significantly as the SFVC increases from 1% to 2%. Therefore, an excessively large SFVC does not significantly improve the force performance of the member while increasing the self-weight of the member due to the incorporation of an excessively large number of fibers. An SFVC of 1% is reasonable considering the advantages offered by lightweight coal gangue concrete.

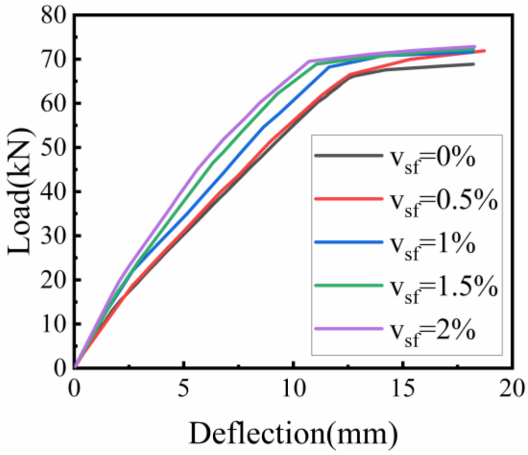

Fig. 25. Simulation results obtained for different SFVCs.

6.6.3. Rebar ratio

The simulated load-deflection curves obtained for rebar ratios of 0.5%, 1.0%, 1.5%, and 2.0% are shown in Fig. 26. With increasing rebar ratio, the ultimate load of SFCGC beam increases significantly but the increase of deflection is less. For SFCGC beams with lower load-carrying capacity than SFOC beams, the load-carrying capacity of SFCGC beams can be improved by increasing the rebar ratio.

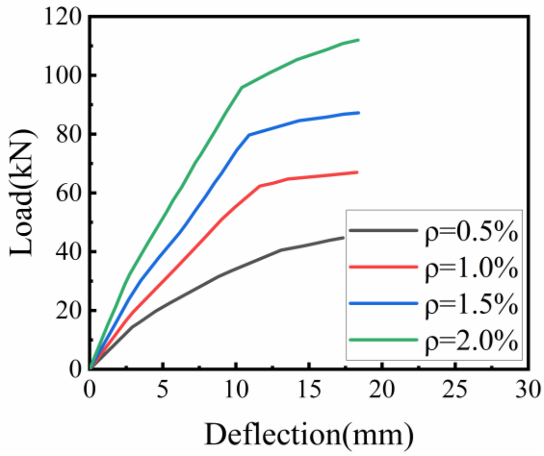

Fig. 26. Simulation results obtained for different rebar ratios.

7. Conclusion

In this study, four-point bending test was conducted on 9 SFCGC beams and 2 SFOC beams. The test parameters were the CGRR, SFVC, rebar ratio, and beam height. The structural properties of the beams, including the flexural stiffness, load-carrying capacity, deformation capacity, cracking behavior, ductility, and energy dissipation, were investigated. The SFCGC beams had comparable structural properties to those of the SFOC beams. The experimental results were compared with those obtained from the FE simulations. The main results of this study are summarized as below.

1) The incorporation of coal gangue aggregates reduces various mechanical properties of the concrete, but the strength of SFCGC beams can be made similar to that of SFOC beams by increasing the rebar ratio and adjusting the mix proportions. Based on the data of axial compression tests on prisms, an equation is proposed to predict the compressive stress-strain constitutive relationship of concrete considering the influence of the CGRR and SFVC.

2) Comparing with SFOC beams, SFCGC beams exhibit low flexural performance, but their strains along the section height still meet the plane section assumption, and their cracking load, yield load, and ultimate load decrease by 8.8%, 12.1%, and 13.3%, respectively, on average.

3) The incorporation of steel fibers effectively delays the development of cracks in SFCGC beams. When the SFVC reaches 1%, the cracking load of SFCGC beams increases by 58.6%, whereas the yield load and ultimate load are minimally affected. When the SFVC exceeds 1%, the cracking load of the specimen increases at a slower rate. For optimal utilization of steel fibers, the optimal SFVC of SFCGC beams should not be greater than 1%.

4) The bearing capacity, stiffness, ductility, and energy dissipation capacity of the SFCGC beams decrease with increasing CGRR and increase with the SFVC, and the CGRR and SFVC have a relatively large influence on the stiffness and ductility. As the rebar ratio increases, the energy dissipation capacity of SFCGC beams first increases and then decreases, and the bearing capacity, stiffness, and ductility of the specimens are enhanced significantly. And the flexural load capacity of SFCGC beam is significantly increased with the increase of beam height.

5) An equation for predicting the constitutive relationship of SFCGC is presented by fitting the test results. The comparative analysis of the test and FE results show that the established FEM can

predict the SFCGC beam flexural performance both reliably and accurately, where there is less than 10% error between the predicted and test results. The influences of the parameters of the CGRR, SFVC, and rebar ratio were analyzed in terms of their effects on the bearing capacity. It is found that the bearing capacity of SFCGC beams is slightly lower than that of SFOC beams; however, the crack resistance and bearing capacity of SFCGC beams can be enhanced by incorporating steel fibers and increasing the rebar ratio.

Data Availability

Some or all data, models, or codes that support the findings of this study are available from the corresponding author upon reasonable request.

Declaration of Competing Interest

The authors declare that they have no known competing financial interests or personal relationships that could have appeared to influence the work reported in this paper.

Acknowledgments

This research was financially supported by the Foundation of China Scholarship Council (No. 201805975002), and a scientific research projects from the Education Department of Jilin Province (JJKH20210279KJ). The authors wish to acknowledge the sponsors. However, any opinions, findings, conclusions and recommendations presented in this paper are those of the authors and do not necessarily reflect the views of the sponsors.

Reference

[1] Quero X, Izquierdo M, Monfort E, Álvarez E, Font O, Moreno T, Alastuey A, Zhuang X, Lu W, Wang Y. Environmental characterization of burnt coal gangue banks at Yangquan, Shanxi Province, China. International Journal of Coal Geology 2008; 75(2), 93-104. https://doi.org/10.1016/j.coal.2008.04.003

[2] Dong Z, Xia J, Fan C, Cao J. Activity of calcined coal gangue fine aggregate and its effect on the mechanical behavior of cement mortar. Construction and Building Materials 2015; 100, 63-69. https://doi.org/10.1016/j.conbuildmat.2015.09.050

[3] Huang G, Ji Y, Li J, Hou Z, Dong Z. Improving strength of calcinated coal gangue geopolymer mortars via increasing calcium content. Construction and Building Materials 2018; 166, 760-768. https://doi.org/10.1016/j.conbuildmat.2018.02.005

[4] Salguero F, Grande J. A, Valente T, Garrido R, De la Torre, M. L., Fortes J. C, Sánchez, A. Recycling of manganese gangue materials from waste-dumps in the Iberian Pyrite Belt–Application as filler for concrete production. Construction and Building Materials 2014; 54, 363-368. https://doi.org/10.1016/j.conbuildmat.2013.12.082

[5] Karimaei M, Dabbaghi F, Sadeghi-Nik A, Dehestani M. Mechanical performance of green concrete produced with untreated coal waste aggregates. Construction and Building Materials 2020; 233, 117264. https://doi.org/10.1016/j.conbuildmat.2019.117264
[6] Yao Z, Fang Y, Kong W, Huang X, Wang X. Experimental study on dynamic mechanical properties of coal gangue concrete. Advances in Materials Science and Engineering 2020; 2020. https://doi.org/10.1155/2020/8874191
[7] Gao S, Zhao G, Guo L, Zhou L, Yuan K. Utilization of coal gangue as coarse aggregates in structural concrete. Construction and Building Materials 2021; 268, 121212. https://doi.org/10.1016/j.conbuildmat.2020.121212
[8] Zhou X.G. Application of fully spontaneous combustion coal clinoptilolite in high-rise frame structure residential building. Building Block & Block Construction 1997; 22–24.
[9] Li D, Song X, Gong C, Pan Z. Research on cementitious behavior and mechanism of pozzolanic cement with coal gangue. Cement and Concrete Research 2006; 36(9), 1752-1759. https://doi.org/10.1016/j.cemconres.2004.11.004
[10] Zhang N, Sun H, Liu X, Zhang J. Early-age characteristics of red mud–coal gangue cementitious material. Journal of Hazardous Materials 2009; 167(1-3), 927-932. https://doi.org/10.1016/j.jhazmat.2009.01.086
[11] Yi C, Ma H, Zhu H, Li W, Xin M, Liu Y, Guo Y. Study on chloride binding capability of coal gangue based cementitious materials. Construction and Building Materials 2018; 167, 649-656. https://doi.org/10.1016/j.conbuildmat.2018.02.071
[12] Qiu J, Zhou Y, Vatin N. I, Guan X, Sultanov S, Khemarak K. Damage constitutive model of coal gangue concrete under freeze-thaw cycles. Construction and Building Materials 2020; 264, 120720. https://doi.org/10.1016/j.conbuildmat.2020.120720
[13] Ma H, Zhu H, Wu C, Chen H, Sun J, Liu J. Study on compressive strength and durability of alkali-activated coal gangue-slag concrete and its mechanism. Powder Technology 2020; 368, 112-124. https://doi.org/10.1016/j.powtec.2020.04.054
[14] Luo D, Wang Y, Zhang S, Niu D, Song Z. Frost resistance of coal gangue aggregate concrete modified by steel fiber and slag powder. Applied Sciences 2020; 10(9), 3229. 10.3390/app10093229
[15] Li Y, Yao Y, Liu X, Sun H, Ni W. Improvement on pozzolanic reactivity of coal gangue by integrated thermal and chemical activation. Fuel 2013; 109, 527-533. https://doi.org/10.1016/j.fuel.2013.03.010
[16] Karagöl F, Yegin Y, Polat R, Benli A, Demirboğa R. The influence of lightweight aggregate, freezing-thawing procedure and air entraining agent on freezing-thawing damage. Structural Concrete 2018; 19(5), 1328-1340. https://doi.org/10.1002/suco.201700133
[17] Zhang Y, & Ling T. C. Reactivity activation of waste coal gangue and its impact on the properties of cement-based materials-a review. Construction and Building Materials 2020; 234, 117424. https://doi.org/10.1016/j.conbuildmat.2019.117424
[18] Hu Q, Fang G. Study on Mechanical Properties of Recycled Concrete Block Mixed with Coal Gangue and Plant Fiber. In IOP Conference Series: Earth and Environmental Science 2020; Vol. 508, No. 1, p. 012179. 10.1088/1755-1315/508/1/012179
[19] Hanant D.J. Fiber Cement and Fiber Concrete. China Architecture & Building Press 1986; Beijing, China.
[20] Marcos-Meson V, Michel A, Solgaard A, Fischer G, Edvardsen C, Skovhus T. L. Corrosion resistance of steel fibre reinforced concrete-A literature review. Cement and Concrete Research

2018; 103, 1-20. https://doi.org/10.1016/j.cemconres.2017.05.016

[21] Park S. H, Kim D. J, Ryu G. S, Koh K. T. Tensile behavior of ultra high performance hybrid fiber reinforced concrete. Cement and Concrete Composites 2012; 34(2), 172-184. https://doi.org/10.1016/j.cemconcomp.2011.09.009

[22] Monetti D. H, Llano-Torre A, Torrijos M. C, Giaccio G, Zerbino R, Martí-Vargas J. R, Serna P. Long-term behavior of cracked fiber reinforced concrete under service conditions. Construction and Building Materials 2019; 196, 649-658. https://doi.org/10.1016/j.conbuildmat.2018.10.230

[23] Thomas J, Ramaswamy A. Mechanical properties of steel fiber-reinforced concrete. Journal of materials in civil engineering 2007; 19(5), 385-392. http://dyuthi.cusat.ac.in/purl/4537

[24] Banthia N, Gupta R. Influence of polypropylene fiber geometry on plastic shrinkage cracking in concrete. Cement and concrete Research 2006; 36(7), 1263-1267. https://doi.org/10.1016/j.cemconres.2006.01.010

[25] Teng S, Afroughsabet V, Ostertag C. P. Flexural behavior and durability properties of high performance hybrid-fiber-reinforced concrete. Construction and Building Materials 2018; 182, 504-515. https://doi.org/10.1016/j.conbuildmat.2018.06.158

[26] Gotame M, Franklin C. L, Blomfors M, Yang J, Lundgren K. Finite element analyses of FRP-strengthened concrete beams with corroded reinforcement. Engineering Structures 2022; 257, 114007. https://doi.org/10.1016/j.engstruct.2022.114007

[27] Aghani K, Afshin H, Abedi K. Finite element-based prediction of the long-term deflection of reinforced concrete beams strengthened with prestressed fiber-reinforced polymers. Structures 2022; Vol. 43, pp. 358-373. https://doi.org/10.1016/j.istruc.2022.06.059

[28] Xu H, Du H, Kang L, Cheng Q, Feng D, Xia S. Constructing straight pores and improving mechanical properties of gangue-based porous ceramics. Journal of Renewable Materials 2021; 9(12), 2129. 10.32604/jrm.2021.016090

[29] Zhang Y, Xu Q, Wang Q, Zhou M, Liu H, Guo H. Axial compressive behavior of circular concrete-filled steel tube stub columns prepared with spontaneous-combustion coal gangue aggregate. Journal of Building Engineering 2022; 103987. https://doi.org/10.1016/j.jobe.2021.103987

[30] Ministry of Housing and Urban-Rural Development, Beijing, China. Specification design of ordinary concrete (JGJ 55-2011). 2011. (in Chinese).

[31] China Association for Engineering Construction Standardization, Beijing, China. Technical specification for fiber reinforced concrete structures (CECS38:2004). 2004. (in Chinese).

[32] Ministry of Housing and Urban-Rural Development, Beijing, China. Standard for test methods of concrete physical and mechanical properties (GB/T 50081-2019). 2019. (in Chinese).

[33] Chu T. C, Ranson W. F, Sutton M. A. Applications of digital-image-correlation techniques to experimental mechanics. Experimental mechanics 1985; 25(3), 232-244.

[34] Systèmes D. Abaqus analysis user’s guide. Solid (Continuum) Elements 2014; 6, 2019.

[35] Guo Z, Shi X. Reinforced concrete theory and analyse. Tsinghua University Press 2003. (in Chinese)

[36] Hillerborg A, Modéer M, Petersson P. E. Analysis of crack formation and crack growth in concrete by means of fracture mechanics and finite elements. Cement and concrete research 1976; 6(6), 773-781.

[37] Ministry of Housing and Urban-Rural Development, Beijing, China. Code for design of concrete structures (GB50010-2010). 2010. (in Chinese).